Chapter 2

New experimental designs and techniques to recover OAM modes from randomness

This chapter presents two different techniques to recover the OAM mode of the helical beam propagating through random scattering media. The details theoretical framework, numerical simulation, and experimental results are also discussed in this chapter.

2.1 Introduction

A light beam with a spiral phase structure $\exp(il\varphi)$ and orbital angular momentum (OAM) of $l\hbar$ (where $\hbar$ is a plank's constant) is referred to as a helical beam (Allen, 2016; Berkhout, 2008; Torres, 2011; Yao, 2006). Term φ represents the azimuthal coordinates and l denotes the TC of the beam (Torres, 2011). A helical beam possesses a central dark core in the amplitude distribution and this arises due to a phase singularity in the helical wavefront (Berkhout, 2008; Yao, 2006). The OAM of the helical beam is a crucial parameter and has shown many interesting applications in optical communication, particle trapping, image processing, diffraction, and optical testing (Gao, 2019; Melo, 2018; Torres, 2011; Willner, 2021). Remarkably, channel strength and spectral efficiency in optical communications are enhanced by OAM encoding and mode multiplexing methods, since OAM modes with various l are theoretically infinite and orthogonal to one another in Hilbert space (Torres, 2011). Hence, to decode the data with various OAM states at the receiver end in OAM communication, a precise estimation of the TC connected with the helical beam is of great indispensable. Till now, a variety of approaches have been established to detect the TC of the helical beam based on interference and diffraction. In the interferometric approach, the interference fringes are recorded to monitor the TC values after a helical beam interferes with a reference beam, such as a plane wave, or spherical wave (Ghai, 2008; Khajavi, 2018; Leach, 2004; Sztul, 2006; Zhao, 2020). However, interferometric systems require complicated optical setups and are sensitive to external disturbances. To overcome this issue, a helical beam was diffracted through a specially designed geometric aperture including a triangular aperture (Araujo, 2011; Melo, 2018), annular gratings (Zheng, 2017), and a translated single slit (Ferreira, 2011).

On the other hand, the existence of a scattering media in the propagation path distorts the wavefront of the incident beam and plays a detrimental role in practical applications (Gong, 2019; Wang, 2015). Propagation of the incident coherent beam in the presence of an inhomogeneous media scrambles the wavefront and generates a granular pattern i.e. speckle (Goodman, 2007). The speckle patterns don't have any direct with the beam and the beam information is scrambled into the spatially fluctuating field. The information-bearing properties of the speckle patterns were examined to develop different detection schemes for the recovery of incident helical beams. Researchers have used coherent light to generate speckle patterns and utilized information-bearing properties of this pattern to develop detection techniques for the recovery and estimation of TC of the helical beam (Acevedo, 2020; Lathika, 2018; Reddy, 2014; Salla, 2015; Vinu, 2014) and in the examination of polarization properties (Singh, R., 2014). In a recent development, the Hanbury-Brown Twiss effect was combined with off-axis holography to estimate the TC of the helical beam. This technique requires a separate reference speckle and an interferometer setup (Vinu, 2016). A distribution of cross-covariance of the random intensity pattern was utilized to estimate the TC by enumerating the number of petals (Chen, 2021). A new method is also demonstrated to recover the OAM states from the highly scattered light using the scattering matrix-assisted retrieval technique (SMART) (Gong, 2019). This works on the determination of the calibrated transmission matrix TM of the complex scattering medium. In addition, some significant detection techniques have been developed in the last decade to detect the TC and spiral phase profile of the helical beam with partially coherent light (Ding, 2014; Lu, 2019; Singh, R., 2015). Recently, incoherent light has also been explored to develop detection schemes for the recovery of TC and spiral phase profile of the helical beam propagating through rough scattering layers (Bezerra, 2020; Huang, 2021; Liu, 2019).

2.2 Stokes fluctuations correlation

Here, we discuss and describe the use of polarization correlations in information recovery and looking through randomness. The basic principle of the technique is explained below.

Consider a transversely polarized monochromatic field with the orthogonal axes x and y coaxially propagating along the z-direction. The complex field at the transverse plane z=0 is represented as

$$E(\hat{r}) = E_x(\hat{r})\hat{e}_x + E_y(\hat{r})\hat{e}_y, \tag{2.1}$$

where $\hat{e}_x$ and $\hat{e}_y$ are horizontal and vertical polarization states of the light respectively and $\hat{r}$ is the spatial position vector at the transverse scattering plane. Now the coherent beam propagates through a random scattering media and reaches an observation plane located at the far field as shown in Fig. 2.1.

$$E(r) = FR\left(E(\hat{r})e^{i\delta(\hat{r})}\right) = \hat{e}_x E_x(r) + \hat{e}_y E_y(r), \tag{2.2}$$

where $E(r)$ denotes the scattered field at the far field, $\delta(\hat{r})$ stands for spatial random phase introduced by non-birefringent random scatterer, r is the spatial position vector at the observation plane and FR represents the Fresnel transform corresponding to propagation at a distance z from the source.

The complex field at the observation plane, located in the Fresnel domain, is given as

$$E(r) = \int G(r,\hat{r})E(\hat{r})e^{i\delta(\hat{r})}d\hat{r}, \tag{2.3}$$

The Green's function $G(r,\hat{r})$ for free-space propagation is

$$G(r,\hat{r}) = \frac{\exp(ikz)}{i\lambda z}\exp\left(ik\frac{|\hat{r}|^2 + |r|^2 - 2\hat{r}.r}{2z}\right) \tag{2.4}$$

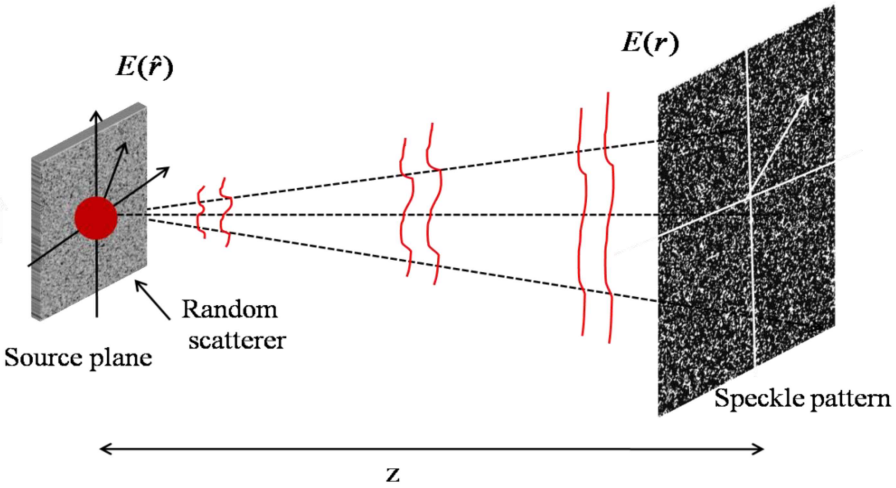

Fig. 2.1 Generation of the speckle pattern.

Therefore, the complex field at the observation plane is represented as

$$E(r) = \frac{\exp(ikz)}{i\lambda z}\exp\left(ik\frac{|r|^2}{2z}\right)\int E(\hat{r})\exp\left(ik\frac{|\hat{r}|^2}{2z}\right)\exp\left(-ik\frac{\hat{r}.r}{z}\right)d\hat{r}, \tag{2.5}$$

where λ and $k = \frac{2\pi}{\lambda}$ are the wavelength and wavenumber of the light, respectively. The Fresnel approximation is utilized by considering a large z value in comparison to the source and the observation area of interest.

To evaluate correlation for a common z plane the coefficient $\frac{\exp(ikz)}{i\lambda z}$ in Eq. (2.5) is ignored from further consideration in the following discussion and the orthogonal polarization components (a, b=x, y) at different spatial observation points are represented as

$$E(r) = \exp\left(ik\frac{|r|^2}{2z}\right)\int E(\hat{r})\exp\left(ik\frac{|\hat{r}|^2}{2z}\right)\exp\left(-ik\frac{\hat{r}.r}{z}\right)d\hat{r},$$

$$E_a^*(r_1) = \exp\left(-ik\frac{|r|^2}{2z}\right)A, \text{where } A = \int E_a^*(\hat{r}_1)\exp\left(-ik\frac{|\hat{r}_1|^2}{2z}\right)\exp\left(ik\frac{\hat{r}_1.r_1}{z}\right)d\hat{r}_1,$$

$$E_b(r_1) = \exp\left(ik\frac{|r_1|^2}{2z}\right)B, \text{where } B = \int E_b(\hat{r}_1)\exp\left(ik\frac{|\hat{r}_1|^2}{2z}\right)\exp\left(-ik\frac{\hat{r}_1.r_1}{z}\right)d\hat{r}_1, \quad (2.6)$$

The correlation function between two orthogonal polarization components of the random field encodes the signature of the light's wavefronts (Vinu, 2016).

A signature of the incident light's wavefront is encoded into a complex polarization correlation function which is obtained from the fluctuations between the SPs of the coherent random field. The SPs are expressed in terms of four Pauli spin matrices (Kuebel, 2019) as

$$S_n(r) = E^{\dagger}(r)\sigma^n E(r), \qquad (n=0, 1, 2, 3), \quad (2.7)$$

where † denotes the Hermitian conjugate, $\sigma^0, \sigma^1, \sigma^2, \sigma^3$ are the 2-by-2 identity matrix and the 2-by-2 three Pauli spin matrices respectively and

$$E(r) = \begin{pmatrix} E_x(r) \\ E_y(r) \end{pmatrix}. \quad (2.8)$$

Hence,

$$S_n(r) = \sum_{a,b}\sigma_{ab}^n E_a^*(r)E_b(r), (a,b = x, y). \quad (2.9)$$

A curvature term in the Fresnel propagation outside the integral ceases to exist after substituting Eq. (2.5) into the Stokes parameters Eq. (2.9).

The fluctuations of the SPs around their average value are defined as

$$\Delta S_n(r) = S_n(r) - < S_n(r) >, \quad (n=0, \ 1, \ 2, \ 3), \tag{2.10}$$

where $S_n(r)$ is the SP at a particular spatial point and $< S_n(r) >$ represents its ensemble average. Assuming spatial stationary and ergodicity in space at the observation plane and we replaced the ensemble average with the spatial average. All possible pairs of 2-point SPs correlation are represented by a 4-by-4 matrix $C_{nm}(\Delta r)$ as follows

$$C_{nm}(\Delta r) = < \Delta S_n(r_1)\Delta S_m(r_1 + \Delta r) >, \quad (n, m=0, 1, 2, 3), \tag{2.11}$$

Elements of the correlations matrix are (Kuebel, 2019; Wu, 2019) as follows

$$\begin{aligned} C_{nm}(\Delta r) &= \left\langle \Delta S_n(r_1)\Delta S_m(r_1 + \Delta r) \right\rangle \\ &= \left\langle S_m(r_1) S_n(r_1 + \Delta r) \right\rangle - \left\langle S_m(r_1) \right\rangle \left\langle S_n(r_1 + \Delta r) \right\rangle \\ &= \sum_{a,b}\sum_{c,d} \sigma_{ab}^{m}\sigma_{cd}^{n} \left\langle E_a^*(r_1) E_b(r_1) E_c^*(r_1 + \Delta r) E_d(r_1 + \Delta r) \right\rangle \\ &\quad - \sum_{a,b} \sigma_{ab}^{n} \left\langle E_a^*(r_1) E_b(r_1) \right\rangle \sum_{c,d} \sigma_{cd}^{m} \left\langle E_c^*(r_1 + \Delta r) E_d(r_1 + \Delta r) \right\rangle. \end{aligned} \tag{2.12}$$

Now, putting the values of $E_a^*(r_1), \mathrm{E_b}(r_1), E_c^*(r_1 + \Delta \mathrm{r})$ and $E_d(r_1 + \Delta \mathrm{r})$ in equation (2.12).

$$C_{nm}(\Delta r) = \sum_{a,b}\sum_{c,d} \sigma_{ab}^{m}\sigma_{cd}^{n} \left\langle \exp\left(-ik \frac{|r_1|^2}{2z} \right) A \exp\left(ik \frac{|r_1|^2}{2z} \right) B \exp\left(ik \frac{|r_1 + \Delta r|^2}{2z} \right) C \right.$$

$$\left. \exp\left(-ik \frac{|r_1 + \Delta r|^2}{\mathbf{2}z} \right) D \right\rangle$$

$$-\sum_{a,b}\sigma_{ab}^{m}\left\langle \exp\left(-ik\frac{|r_1|^2}{2z}\right)A\exp\left(ik\frac{|r_1|^2}{2z}\right)B\right\rangle\sum_{c,d}\sigma_{cd}^{m}\left\langle \exp\left(ik\frac{|r_1+\Delta r|^2}{2z}\right)C\right.$$

$$\left.\exp\left(-ik\frac{|r_1+\Delta r|^2}{2z}\right)D\right\rangle$$

$$=\sum_{a,b}\sum_{c,d}\sigma_{ab}^{m}\sigma_{cd}^{n}\langle ABCD\rangle-\sum_{a,b}\sigma_{ab}^{m}\langle AB\rangle\sum_{c,d}\sigma_{cd}^{n}\langle CD\rangle, \tag{2.13}$$

where the right-hand side of the above equation represents the sum of products of second-order correlations. Equation (2.13) shows that phase curvature outside the integral in Eq. (2.5) can be ignored in the higher-order SPs correlations.

Now, applying the moment theorem for a Gaussian random process (Singh, 2013; Takeda, 2014), the 4 x 4 Stokes fluctuations correlations matrix can be expressed as

$$C_{nm}(\Delta r)=\sum_{a,b}\sum_{c,d}\sigma_{ab}^{m}\sigma_{cd}^{n}\left[\langle AB\rangle\langle CD\rangle+\langle AD\rangle\langle CB\rangle\right]-\sum_{a,b}\sum_{c,d}\sigma_{ab}^{m}\sigma_{cd}^{n}\langle AB\rangle\langle CD\rangle$$

$$=\sum_{a,b}\sum_{c,d}\sigma_{ab}^{m}\sigma_{cd}^{n}\langle AD\rangle\langle CB\rangle$$

$$=\sum_{a,b}\sum_{c,d}\sigma_{ab}^{n}\sigma_{cd}^{m}W_{ad}(\Delta r)W_{bc}^{*}(\Delta r),\quad (a,\,b,\,c,\,d=x,\,y), \tag{2.14}$$

where,

$$\langle AD\rangle=W_{ad}(\Delta r)=\iint\left[\int\exp\left(\frac{ik}{2z}[|\hat{r}_2|^2-|\hat{r}_1|^2]\right)\exp\left(\frac{-ik}{z}[(r_1+\Delta r_1).\hat{r}_2-r_1.\hat{r}_1]\right)[E_a^{*}(\hat{r}_1)\right.$$

$$\left.E_d(\hat{r}_2)\right]dr\Big]d\hat{r}_1d\hat{r}_2,$$

$$\langle CB\rangle=W_{bc}^{*}(\Delta r)=\iint\left[\left\{\exp\left(\frac{ik}{2z}[|\hat{r}_2|^2-|\hat{r}_1|^2]\right)\exp\left(\frac{-ik}{z}[(r_1+\Delta r_1).\hat{r}_2-r_1.\hat{r}_1]\right)[E_b^{*}(\hat{r}_1)\right.\right.$$

$$E_c(\hat{r}_2)\Big]dr\Big\}d\hat{r}_1 d\hat{r}_2\Big]^*,$$

By using the relation $\int \exp\left(-\frac{ik}{z}(\hat{r}_2-\hat{r}_1).r_1\right)dr_1 = \delta(\hat{r}_2-\hat{r}_1).$

$$W_{ad}(\Delta r) = \int [E_a^*(\hat{r}_1)E_d(\hat{r}_1)]\exp\left[-i\frac{2\pi}{\lambda z}\Delta r.\hat{r}_1\right]d\hat{r}_1, \tag{2.15}$$

$$W_{bc}^*(\Delta r) = \int [E_b^*(\hat{r}_1)E_c(\hat{r}_1)]^*\exp\left[i\frac{2\pi}{\lambda z}\Delta r.\hat{r}_1\right]d\hat{r}_1, \tag{2.16}$$

where $E_a^*(\hat{r}_1)E_d(\hat{r}_1)$, $E_b^*(\hat{r}_1)E_c(\hat{r}_1)$, denote polarization source structure at the diffuser plane. The polarization correlation at the observation plane is the Fourier transform of the source at the diffuser plane. We would like to emphasize that the fourth-order correlation permits achieving spatial stationarity even in the Fresnel domain and permits the lensless Fourier transform relation between the random source and coherence at the observation plane at any arbitrary distance z.

Elements of the correlation matrix for the polarized light in Eq. (2.14) are obtained by considering spatial averaging. The correlations between the SPs fluctuations are explained by equation (2.14) which provides sixteen terms.

$$C_{00}(\Delta r) = |W_{xx}(\Delta r)|^2 + |W_{xy}(\Delta r)|^2 + |W_{yx}(\Delta r)|^2 + |W_{yy}(\Delta r)|^2, \tag{2.17}$$

$$C_{01}(\Delta r) = |W_{xx}(\Delta r)|^2 - |W_{xy}(\Delta r)|^2 + |W_{yx}(\Delta r)|^2 - |W_{yy}(\Delta r)|^2, \tag{2.18}$$

$$C_{02}(\Delta r) = 2\,\mathrm{Re}\left[W_{xx}(\Delta r)W_{xy}^*(\Delta r) + W_{yy}(\Delta r)W_{yx}^*(\Delta r)\right], \tag{2.19}$$

$$C_{03}(\Delta r) = 2Im\left[W_{yy}(\Delta r)W_{yx}^*(\Delta r) - W_{xx}(\Delta r)W_{xy}^*(\Delta r)\right], \tag{2.20}$$

$$C_{10}(\Delta r) = |W_{xx}(\Delta r)|^2 + |W_{xy}(\Delta r)|^2 - |W_{yx}(\Delta r)|^2 - |W_{yy}(\Delta r)|^2, \tag{2.21}$$

$$C_{11}(\Delta r) = |W_{xx}(\Delta r)|^2 - |W_{xy}(\Delta r)|^2 - |W_{yx}(\Delta r)|^2 + |W_{yy}(\Delta r)|^2, \quad (2.22)$$

$$C_{12}(\Delta r) = 2\,\mathrm{Re}\left[W_{xx}(\Delta r)W_{xy}^{*}(\Delta r) - W_{yy}(\Delta r)W_{yx}^{*}(\Delta r)\right], \quad (2.23)$$

$$C_{13}(\Delta r) = 2\,Im\left[W_{xy}(\Delta r)W_{xx}^{*}(\Delta r) + W_{yx}(\Delta r)W_{yy}^{*}(\Delta r)\right], \quad (2.24)$$

$$C_{20}(\Delta r) = 2\,\mathrm{Re}\left[W_{xx}(\Delta r)W_{yx}^{*}(\Delta r) + W_{yy}(\Delta r)W_{xy}^{*}(\Delta r)\right], \quad (2.25)$$

$$C_{21}(\Delta r) = 2\,\mathrm{Re}\left[W_{xx}(\Delta r)W_{yx}^{*}(\Delta r) - W_{yy}(\Delta r)W_{xy}^{*}(\Delta r)\right], \quad (2.26)$$

$$C_{22}(\Delta r) = 2\,\mathrm{Re}\left[W_{xx}(\Delta r)W_{yy}^{*}(\Delta r) + W_{xy}(\Delta r)W_{yx}^{*}(\Delta r)\right], \quad (2.27)$$

$$C_{23}(\Delta r) = 2\,Im\left[W_{xy}(\Delta r)W_{yx}^{*}(\Delta r) + W_{yy}(\Delta r)W_{xx}^{*}(\Delta r)\right], \quad (2.28)$$

$$C_{30}(\Delta r) = 2\,Im\left[W_{xx}(\Delta r)W_{yx}^{*}(\Delta r) - W_{yy}(\Delta r)W_{xy}^{*}(\Delta r)\right], \quad (2.29)$$

$$C_{31}(\Delta r) = 2\,Im\left[W_{xx}(\Delta r)W_{yx}^{*}(\Delta r) + W_{yy}(\Delta r)W_{xy}^{*}(\Delta r)\right], \quad (2.30)$$

$$C_{32}(\Delta r) = 2\,\mathrm{Im}\left[W_{xy}(\Delta r)W_{yx}^{*}(\Delta r) + W_{xx}(\Delta r)W_{yy}^{*}(\Delta r)\right], \quad (2.31)$$

$$C_{33}(\Delta r) = 2\,\mathrm{Re}\left[W_{xx}(\Delta r)W_{yy}^{*}(\Delta r) - W_{xy}(\Delta r)W_{yx}^{*}(\Delta r)\right], \quad (2.32)$$

Now the different combinations of the elements of the complex polarization correlation matrix are considered to develop and design OAM mode recovery techniques.

2.3 Higher order Stokes parameters correlation

Higher-order correlation of the Stokes parameters (SPs) of the randomly scattered field is implemented to quantitatively measure the topological charge and phase structure of the incident vortex beam propagating through random scattering media as shown in Fig 2.2. Only four elements $C_{20}(\Delta r)$, $C_{21}(\Delta r)$, $C_{30}(\Delta r)$, and $C_{31}(\Delta r)$, are used to make a new theoretical basis to retrieve the OAM mode of the incident light from the random light. The advantage of our technique lies in its ability to recover the incident OAM modes in a completely non-interferometric way. Here, we use a strategy of polarization guiding to

faithfully deliver information through a random scattering medium and our scheme is sketched in Fig. 2.2.

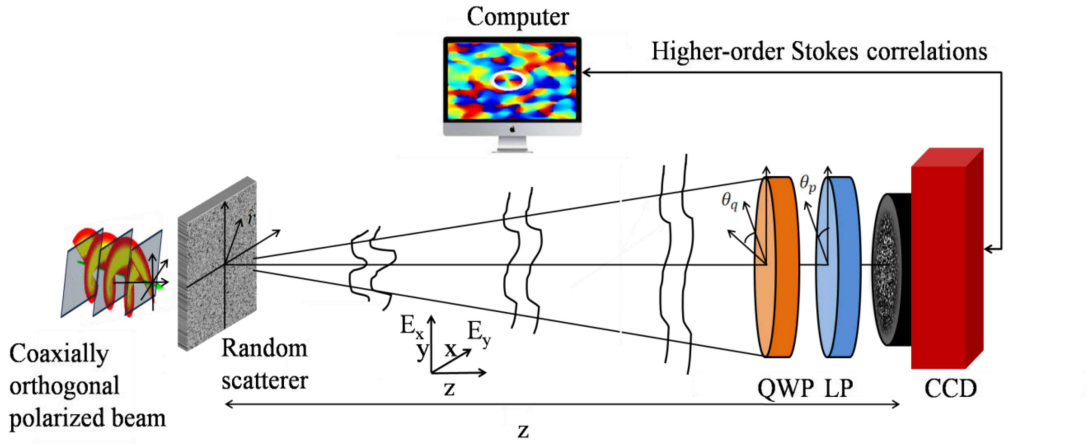

Fig. 2.2 Conceptual representation of the proposed technique with OAM mode and polarization guiding. Generation of random electromagnetic fields by orthogonally polarized light. x and y polarization components represent helical and non-helical wavefronts of the incident light. A CCD records intensity speckle patterns at the observation plane. These speckle patterns are used to determine four SPs and subsequently, higher-order SPs correlations provide the structure of the incident helical wavefront.

Our non-interferometric and iteration-free approach offers simple and stable solutions against external disturbances and vibrations. We have built a completely new theoretical approach based on our work strategy, and an experimental test is carried out to examine and confirm our proposed theoretical basis. Moreover, a simulation model of the experimental situation is also realized and these results are confirmed with the experimental results. The application of our technique is demonstrated in the recovery of the twisted wavefront and OAM modes of the incident light propagating through a random scattering medium. Details of the theoretical basis, numerical simulation, and experimental implementation are discussed below.

2.3.1 Theoretical basis

We examine the role of the complex polarization correlation functions (CPCF) from

equations (2.25), (2.26), (2.29), and (2.30) in the recovery of OAM mode. The real part of the CPCF can be obtained by adding equations (2.25) and (2.26). Similarly adding equations (2.29) and (2.30) provides an imaginary part of the CPCF. In order to use the CPCF for the recovery of OAM mode, the x-polarized state of the light is loaded with a helical beam i.e $E_x(\hat{r}) = A_l(\hat{r})\exp[il\varphi]$, where $A_l(\hat{r})$ represents the amplitude of the helical beam, l is the topological charge (TC) and φ indicates azimuthal coordinate, while the y-polarized state is free from a helical beam i.e $E_y(\hat{r}) = A(\hat{r})$. Therefore, the CPCF is recovered from real and imaginary parts as follows:

$$C(\Delta r) = C_{\mathrm{Re}}(\Delta r) + iC_{\mathrm{Im}}(\Delta r)$$

$$= \left[C_{20}(\Delta r) + C_{21}(\Delta r)\right] + i\left[C_{30}(\Delta r) + C_{31}(\Delta r)\right]$$

$$= 4\,\mathrm{Re}\left[W_{xx}(\Delta r)W_{yx}^{*}(\Delta r)\right] + i4\,\mathrm{Im}\left[W_{xx}(\Delta r)W_{yx}^{*}(\Delta r)\right], \tag{2.33}$$

where $$W_{xx}(\Delta r) = \int [A_l^{*}(\hat{r}_1)A_l(\hat{r}_1)]\exp\left[-i\frac{2\pi}{\lambda z}\Delta r.\hat{r}_1\right]d\hat{r}_1, \tag{2.34}$$

and $$W_{yx}(\Delta r) = \int \left\{A^{*}(\hat{r}_1)A_l(\hat{r}_1)\exp[il\varphi]\right\}\exp\left[-i\frac{2\pi}{\lambda z}\Delta r.\hat{r}_1\right]d\hat{r}_1, \tag{2.35}$$

where, $C_{Re}(\Delta r)$, $C_{Im}(\Delta r)$ represent real and imaginary parts of the CPCF respectively, and $C(\Delta r)$ represents the CPCF. Equation (2.33) is our main result and is utilized for quantitative recovery of the OAM mode from the randomly scattered light. In order to recover the incident OAM modes of the light, we design a system where the correlation function of the x polarization component, i.e. $W_{xx}(\Delta r)$ is considered to be uniform and covers the support of $W_{yx}^{*}(\Delta r)$. This helps us to recover the complex correlation function $W_{yx}^{*}(\Delta r)$ from the measurement of the SPs and subsequently in retrieving the OAM mode

from the randomly scattered light.

2.3.2 Simulation results

To illustrate the feasibility of the proposed technique, we have simulated the different OAM modes of the helical beam with TC l = 1, 2, and 3 and their propagation through a random scattering medium in a polarization guiding condition as sketched in Fig. 2.2. Simulation is performed for a diagonally polarized light field with wavelength $\lambda = 632.8$ nm. The helical beam is loaded into the x-polarized component while the y-polarized component is free from a helical beam and they launched coaxially into the random scattering medium. The random phase screens with phase variation with equal probability distribution in the range of $[-\pi, \pi]$ are used to model random scattering and propagation of the coaxially orthogonal polarization states through such scatterers. A random field from the scattering media propagates from the source to the observation plane at z=250 mm and is modeled using a Fresnel propagation kernel. The Stokes parameters of the random field at the observation plane z=250 mm are evaluated from the digitally propagated coherent random fields. The higher-order Stokes fluctuations correlations as explained in Eq. (2.11) are obtained from these simulated SPs and utilized to estimate the OAM mode. The elements of the polarization correlation matrix $C_{20}(\Delta r), C_{21}(\Delta r), C_{30}(\Delta r),$ and $C_{31}(\Delta r)$ are calculated by using Eq. (2.14) under the consideration of the spatial stationarity at the observation plane and using spatial averaging as a replacement for ensemble averaging. Digital evaluation of the cross-covariance of the SPs is obtained by spatial averaging under the condition of spatial ergodicity. This is implemented by selecting a portion of the SP as a matrix $S_n^{\alpha}(x, y)$ which represents one realization of the SP of the random field. Here x and y are the pixel spatial coordinates and take values up to 300x300 pixels. The cross-covariance of the SPs

for the different realization of the random patterns and this process is represented as $\sum_{\alpha=1}^{M}[\Delta S_m^{\alpha}(x,y)\Delta S_n^{\alpha}(0,0)]/M$. Here, M denotes the number of different realizations of the matrix $S_n^{\alpha}(x,y)$ arising due to pixel-by-pixel movement of the matrix $S_n^{\alpha}(x,y)$ over the SP.

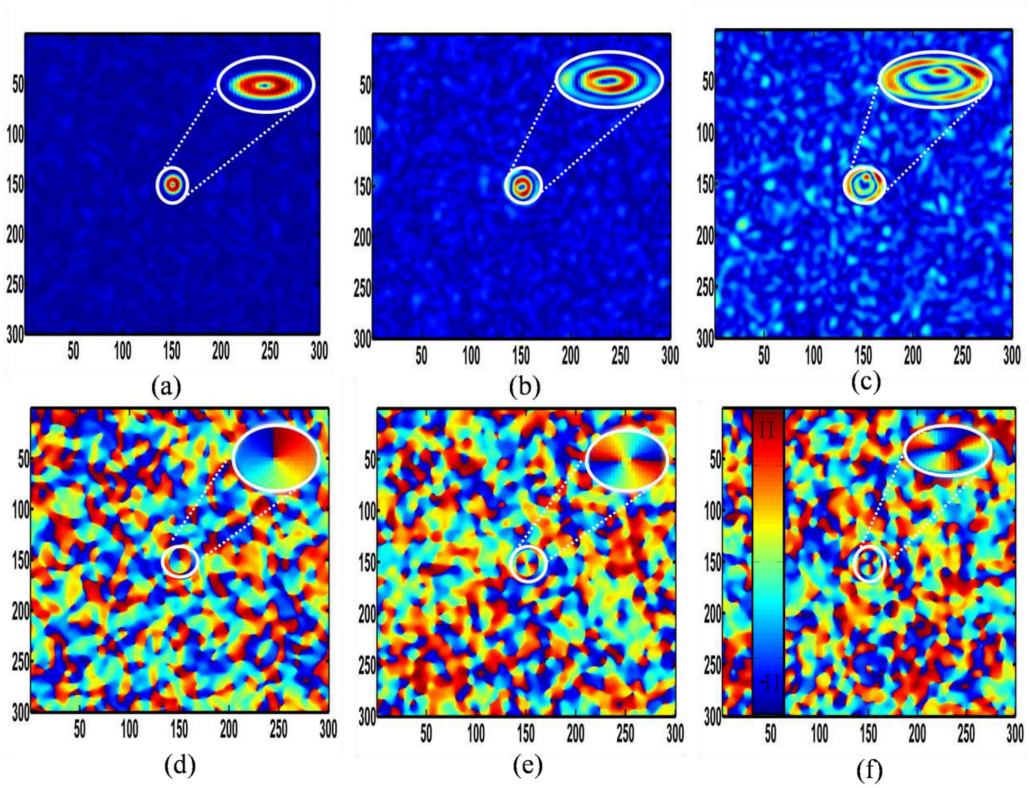

Fig. 2.3 Simulation results; **(a-c)** amplitude distribution of complex polarization correlation function for three different cases**, (d-f)** are the corresponding phase distribution.

We have considered a random pattern of size 1000 x1000 pixels and two-dimensional scanning of $S_n^{\alpha}(x,y)$ over the random pattern provides 700x700 different realizations for averaging. Finally, the CPCF is evaluated from these elements and helps to extract the information about the OAM mode of the helical beams. Fig. 2.3 shows the simulation results of the helical beam with TC *l=1, 2, 3*. For a given l, the helical beam shows intertwined twisted phase wavefronts, which share left-handedness (or right-handedness)

with positive (or negative) l, and a ring-shaped intensity profile. Also Figs. 2.3, (a-c) show that the radius of the 'doughnut-shaped distribution increases with l. The helical phase structures of the coherent vortex beam can be revealed and quantitatively measured from the phase distribution of the CPCF as in Figs. 2.3. This specifies the phase structure of the incident helical beam and demonstrates that the piled-up phase varies around the singularity in the order of $2l\pi$ ($l = 1, 2, 3$ for three topological charges). This technique also determines the sign of the twisted wavefront from the experimentally detected helical structure.

2.3.3 Experiment and results discussions

In order to demonstrate recovery of the topological charge and twisted wavefront of the incident helical beam from the speckle, we designed an experimental set-up as shown in Fig. 2.4. A spatially filtered collimated He-Ne laser light beam is attenuated with a neutral density filter (NDF) and oriented at $45°$ with respect to the horizontal direction using a half-wave plate (HWP). The $45°$ polarized beam splits into two equal-intensity beams by the beam splitter BS. A beam transmitted from BS illuminates a phase-only SLM with a resolution of 1920 x 1080 and a pixel pitch of 8 μm (Pluto from Holoeye) on which the structure of the helical beam is displayed. Consequently, the structure of the vortex information is loaded into the x-polarization component of the beam and the y-polarization component remains intact, i.e., no helical wavefront. The beam coming from the SLM reflects by the BS and travels through the ground glass and random scattering from the ground glass (GG) distorts the incident light encoded with the helical beam and generates a speckle pattern. In order to detect the polarization states of the randomly scattered light, we use optical elements to measure the SPs. The random light further passes through a QWP, which is rotated at an angle θ_q with respect to the x-direction and

filtered by an LP. The transmission axis of the LP is placed in the x-direction with respect to the QWP and the resultant field is captured by a CCD camera with a dynamic range of 8-bit and resolution of 1280 x 1024 pixels and a pixel pitch of 4.65 microns [Thorlab model No. DCU224M] which was placed at a distance, z= 250 mm from the diffuser. The intensity speckle patterns are recorded by the CCD camera. The four SPs shown in Fig. 2.5 are determined from the recorded speckle patterns by using the following equations (Brundavanam, 2012).

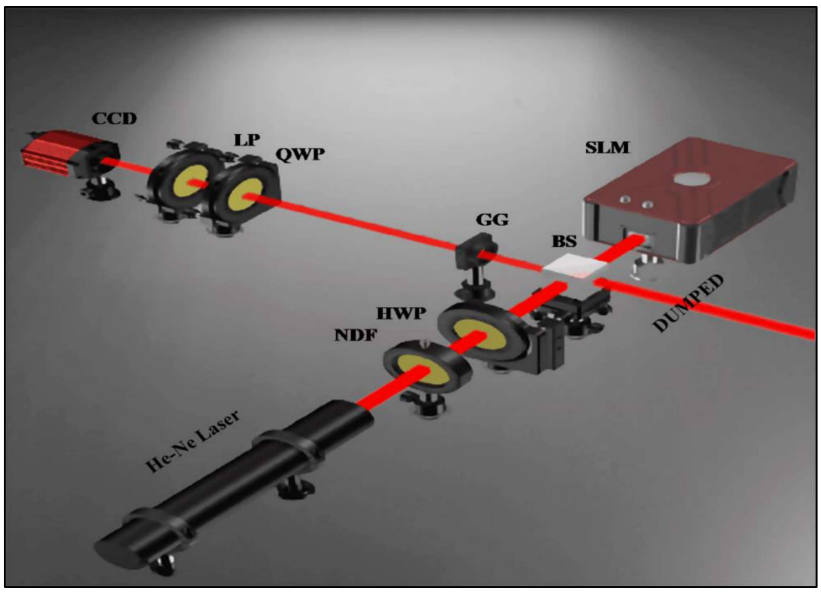

Fig. 2.4 An experimental setup to detect twisted wavefront from the randomly scattered intensity. NDF: neutral density filter, HWP: half-wave plate, BS: beam splitter, SLM: spatial light modulator, GG: ground glass, QWP: quarter-wave plate, LP: linear polarizer, CCD: charge-coupled device. The dumped beam is not used in the experiment.

$$
\begin{aligned}
S_0(r) &= I(0^0,0^0) + I(90^0,90^0),\\
S_1(r) &= I(0^0,0^0) - I(90^0,90^0),\\
S_2(r) &= I(45^0,45^0) - I(135^0,135^0),\\
S_3(r) &= I(0^0,45^0) - I(0^0,135^0),
\end{aligned}
\tag{2.36}
$$

where $I(\theta_q, \theta_p)$ is the intensity at the observation plane. θ_q is the orientation of the optic axis of the quarter-wave plate with the axis of the polarizer and θ_p is the angle of the

polarizer with the x-axis.

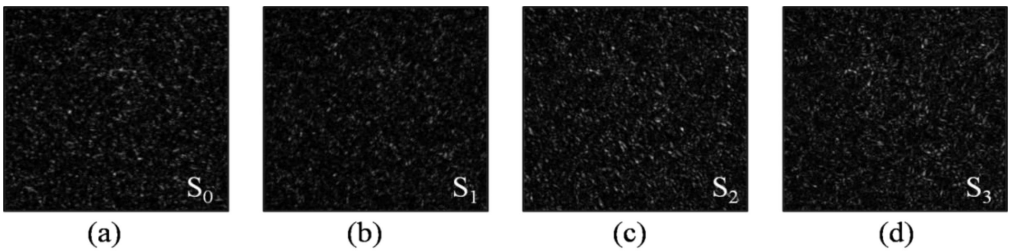

Fig. 2.5 Experimentally measured SPs.

The correlations of the fluctuations of the SPs are determined from the experimentally measured SPs as explained in the theory and simulation section. Digital evaluation of the cross-covariance of the experimentally detected SPs is obtained by spatial averaging under the condition of spatial ergodicity and the process of spatial averaging is explained in the previous section. The real and imaginary parts of the two-point complex polarization function are digitally obtained from the digital correlations of the Stokes parameters as described in the theory section and explained by using Eq. (2.33). The complex correlation function of the orthogonal polarization component is obtained as explained in Eq. (2.33). An incident vortex beam scrambled by the scattering medium is encoded into the complex coherence function $W_{yx}^{*}(\Delta r)$ as described in Eq. (2.33). Experimental results of the incident OAM modes are shown in Fig. 2.6. Figs. 2.6, (a-c) represent amplitude distribution, and (d-f) represent phase distribution of $W_{yx}^{*}(\Delta r)$ for three TC values $l = 1,2,3$. The reconstruction quality of the coherent vortex beam is affected by a high TC. These results are due to the small-sized QWP and LP in the experimental set-up which provides a limited number of speckle grains in the camera plane. This can be resolved with bigger-size polarization optics.

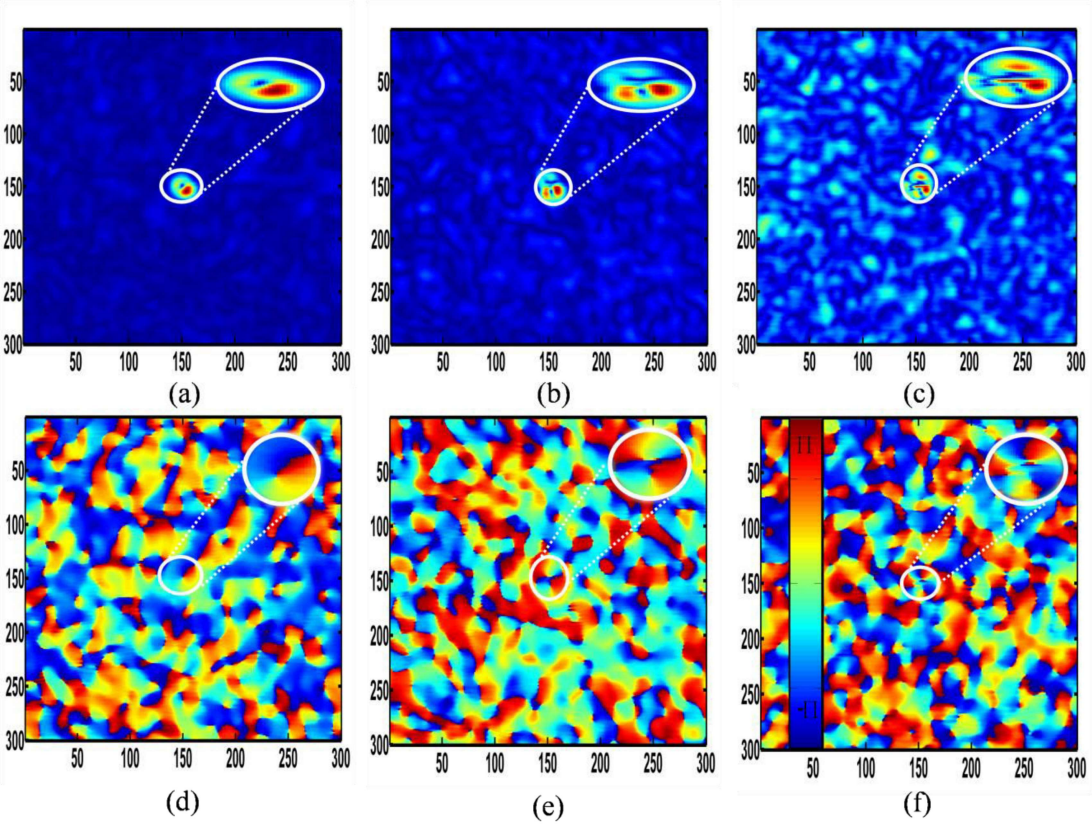

Fig. 2.6 Simulation results; **(a-c)** amplitude distribution of complex polarization correlation function for three different cases, **(d-f)** are the corresponding phase distribution.

2.3.4 Mode analysis

The orthogonal projection method is used to further investigate the incident OAM modes from the scattered light. The coherence polarization correlation function $C(\Delta r)$ encodes the incident helical modes. To examine the incident optical signal encoded into the x polarization component with a polarization guiding condition, we applied projection of $C(\Delta r)$ into spiral harmonics$e^{il\varphi}$, where l is the topological charge. Such projection methods can be used to investigate the angular momentum content of the field distribution (D'Errico, 2017; Molina-Terriza, 2001).

To obtain the OAM power spectrum, first, an angular Fourier transform with respect to

the azimuthal angle is applied over $C(\Delta r)$ to determine complex coefficients A_m. The complex coefficient $A_m$is associated with each OAM value as a function of the radial coordinates. Then a numerical integration with respect to the radial coordinates is used over the modulus square of A_m to determine the OAM power spectrum of the beam. Eventually, the OAM power spectrum is used to decompose each OAM component in terms of azimuthal modes, e.g. helicity (Molina-Terriza, 2001).

The angular Fourier transform of the CPCF is used to define the complex coefficient A_m.

$$A_m = \frac{1}{2\pi}\int_0^{2\pi} d\varphi e^{-il\varphi}\, C(\Delta r). \tag{2.37}$$

The OAM power spectrum of the incident coherent beam is obtained from the complex coefficient by integrating their square modulus along with the radial coordinates.

$$P(l) = \frac{1}{S}\int_0^{\infty} drr|A_m|^2, \tag{2.38}$$

where, $S = \sum\int_0^{\infty} drr|A_m|^2$ is the beam power and $P(l)$ represents the OAM power spectrum.

Simulation and experimental results of the OAM distributions are shown in Fig. 2.7. Figs. 2.7, (a-c), and (d-f) represent simulation and experimental results respectively. In Figs. 2.7, (a-c), and (d-f), the red and blue color bars reveal the OAM distribution for three different OAM modes $l = 1,2,3$ respectively.

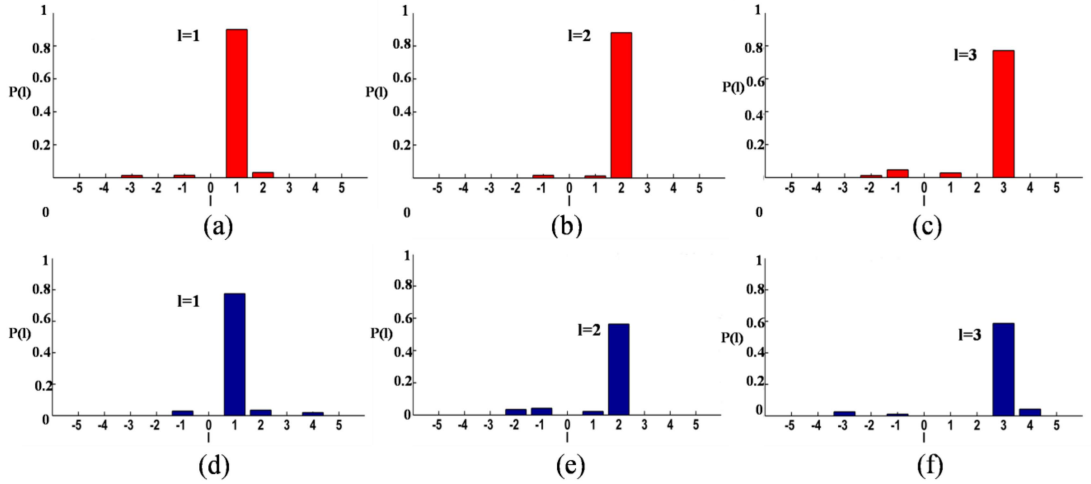

Fig. 2.7 Panels **(a-c), (d-f)** represent simulation and experimental results for the OAM distribution for three different OAM modes $\boldsymbol{l = 1, 2, 3}$.

2.4 Digital phase-shifting with Stokes correlation

Phase-shifting interferometry is a fascinating and powerful tool to analyze interferograms to recover phase information (Groot, 2011). Traditionally, interferograms are measured by locating the center of the fringe and then tracing along the fringe. Phase-shifting interferometry does not require tracing the location of the fringes and enables a point-by-point reconstruction of the wavefront as shown in Fig. 2.8.

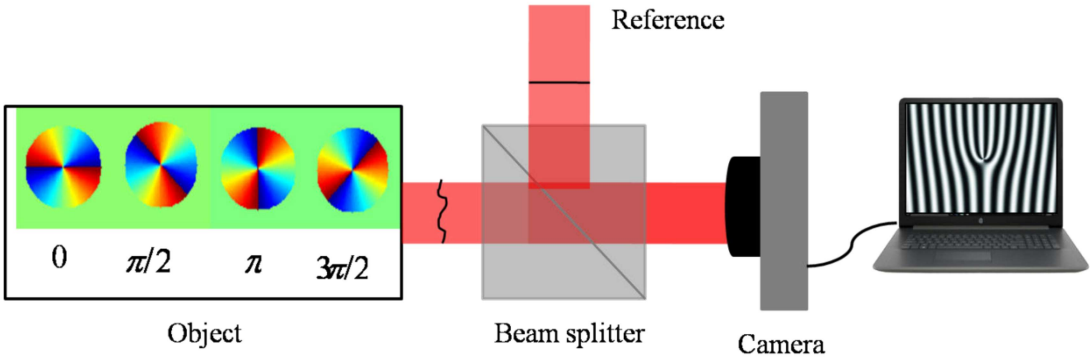

Fig. 2.8 Schematic for conventional phase-shifting technique.

Consider an interference of coherent waves coming from an object $E_o(r)$ and reference

$R(r)$ at the detection plane. The intensity is denoted as

$$I(r) = I_1(r) + I_2(r) + 2\sqrt{I_1(r)I_2(r)}\cos\left[\varphi(r) + \varphi_c\right], \tag{2.39}$$

where $I_1(r) = |E_o|^2$, and $I_2(r) = |R(r)|^2$. $\varphi(r)$ is the phase being measured and φ_c represents phase shifts. The phase $\varphi(r)$ is recovered using phase-shifting interferometry by recording multiple interferograms with different values of φ_c. The phase-shifting technique has a wide range of applications in adaptive optics (Chung, 2006), profilometry (Groot, 2011), holography (Yamaguchi, 2006), etc.

On the other hand, the coherence function follows the same wave equation as the optical field (Takeda, 2021). The wave nature of the coherence function and the interference of the coherence wave were utilized to develop and design various correlation-based quantitative phase imaging and coherence synthesis techniques (Singh, R., 2014). Recently, a few phase-shifting speckle holography techniques with second and higher-order correlation have been investigated for phase recovery through the scattering media (Chen, 2020; 2021; 2022). However, all these techniques demand the interference of the coherence wave to recover the phase.

Here, we developed a non-interferometric phase-shifting technique for the coherence wave using polarization correlation to quantitatively recover the helical wavefront from the scattered light as depicted in Fig. 2.9. In this technique, the combination of the phase-shifting along with the correlations of only the first three SPs helps to unscramble the helical wavefront. A theoretical basis is developed to unscramble the helical wavefront of the incident coherent beam from a speckle pattern. Moreover, this is implemented in a lensless configuration using higher-order SPs correlations. Only two elements $C_{20}(\Delta r)$, and $C_{21}(\Delta r)$ are used to restore the real part of the polarization

correlation function and subsequently applied in unscrambling the helical wavefronts from the random field. To exploit the advantages of phase-shifting along with the SPs correlations, a phase shift is introduced in one of the polarization components of the helical wavefront. The advantage of our technique lies in its ability to unscramble the incident helical wavefront in a completely non-interferometric way, with lensless configuration, and free from the use of a QWP. The QWP is sensitive to mechanical rotation and placing QWP in the Stokes polarimetry influences the state of polarization (SOP) measurements due to the absorption of light hence needs careful calibration (Schaefer, 2007). The developed theoretical basis is experimentally tested and verified by experimental results. The application of our technique is demonstrated in unscrambling the incident helical wavefront propagating through a complex random scattering medium for two different cases. The theoretical approach, simulation results, and experimental implementation are discussed below.

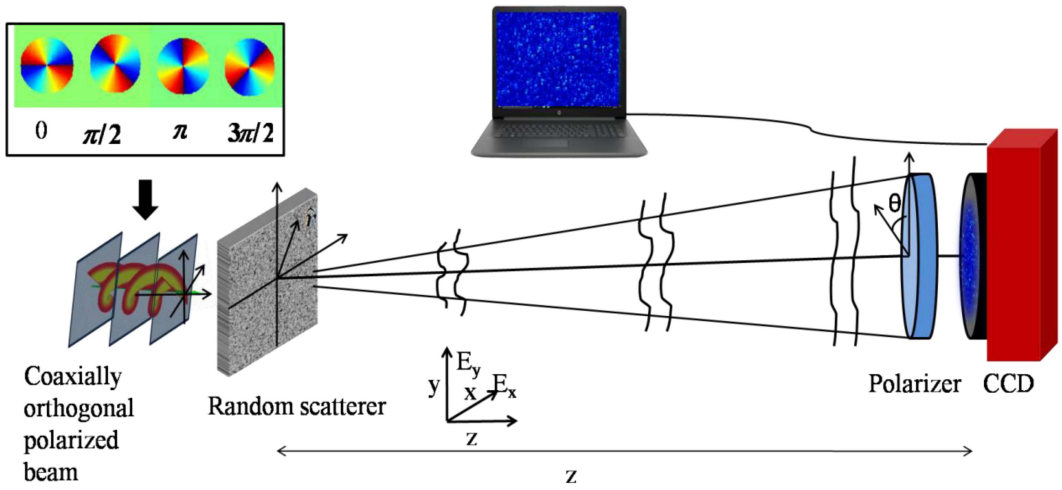

Fig. 2.9 Conceptual sketch of the four-phase shifting technique for coherence wave.

2.4.1 Theoretical model

The real part of the CPCF is evaluated by adding equations (2.25) and (2.26). To recover

the helical wavefront, the x-polarized component of the light is encoded with a helical beam i.e $E_x(\hat{r}) = A_l(\hat{r})\exp\left[i(l\varphi_i - \varphi_c)\right]$, where $A_l(\hat{r})$ is the amplitude distribution of the vortex beam. φ_i, l denote azimuthal coordinate and azimuthal mode index (TC) respectively. φ_c is the constant phase shift and the y-polarized state carries a non-helical beam with uniform amplitude i.e $E_y(\hat{r}) = A_0(\hat{r})$. The real part of the CPCF is calculated as

$$C_{\mathrm{Re}}(\Delta r) = C_{20}(\Delta r) + C_{21}(\Delta r)$$

$$= 4\,\mathrm{Re}\left[W_{xx}(\Delta r)W_{yx}^{*}(\Delta r)\right], \tag{2.40}$$

where $$W_{xx}(\Delta r) = \int [A_l^{*}(\hat{r}_1)A_l(\hat{r}_1)]\exp\left[-i\frac{2\pi}{\lambda z}\Delta r.\hat{r}_1\right]d\hat{r}_1, \tag{2.41}$$

$$W_{yx}(\Delta r) = \int \left\{A^{*}(\hat{r}_1)A_l(\hat{r}_1)\exp\left[i(l\varphi_i - \varphi_c)\right]\right\}\exp\left[-i\frac{2\pi}{\lambda z}\Delta r.\hat{r}_1\right]d\hat{r}_1, \tag{2.42}$$

Now, we digitally introduce phase-shift into one of the polarization states of the incident beam and apply the four-step phase-shifting formula to unscramble the helical phase of the incident beam (Chen, 2020).

$$\varphi_i = \tan^{-1}\left(\frac{C_{\mathrm{Re}}^{3\pi/2}(\Delta r) - C_{\mathrm{Re}}^{\pi/2}(\Delta r)}{C_{\mathrm{Re}}^{0}(\Delta r) - C_{\mathrm{Re}}^{\pi}(\Delta r)}\right), \tag{2.43}$$

where, $C_{Re}^{\frac{3\pi}{2}}(\Delta r)$, $C_{Re}^{\pi}(\Delta r)$, $C_{Re}^{\frac{\pi}{2}}(\Delta r)$, and $C_{Re}^{0}(\Delta r)$ indicate the real part of the Stokes fluctuations correlation function of phase shifts of $3\pi/2, \pi, \pi/2$, and 0 respectively. Using Eq. (2.43) the complex field of the incident helical beam is recovered from the non-imaged speckle pattern and represented as $A(\hat{r})e^{il\varphi_i}$. This term represents the experimentally measured helical wavefront of the beam. To unscramble the helical wavefront of the incident light, we introduced a four-step digital phase-shifting technique.

This is realized by a system where the correlation function of the x polarization component, i.e. $W_{xx}(\Delta r)$ is considered to be uniform and covers the support of $W_{yx}^{*}(\Delta r)$. This helps us to recover the real part of the complex polarization correlation function from the first three SPs with phase shifts of 0, $\pi/2$, π, and $3\pi/2$. Finally, the helical phase structure of the incident beam is retrieved by applying Eq. (2.43).

2.4.2 Simulation results

To validate the proposed technique, we have simulated the different helical beams with TC l = 1, and 2. Simulation is performed for coaxially propagating orthogonally polarized light with wavelength $\lambda = 632.8\,\text{nm}$. The helical beam is encoded into the x-polarized state and the y-polarized carries a non-helical beam with uniform amplitude. A random field of the coaxially orthogonal polarization states is generated by considering a random phase screen with phase variation with equal probability distribution in the range of $[-\pi, \pi]$. The Fresnel propagation kernel is used to model the propagation of the random field from the scattering media to the observation plane at z=250 mm. The Stokes parameters of the random field at the observation plane z=250 mm are measured from the digitally propagated coherent random fields. The higher-order Stokes fluctuations correlations as explained in Eq. (2.11) are evaluated from these simulated SPs and explored to unscramble helical wavefront. Finally, the real part of the CPCF and subsequently, the helical wavefront is recovered from the random light using Eq. (2.40) & Eq. (2.43). Fig. 2.10 shows the simulation results of the recovered helical wavefront with TC l=1, 2. Figs. 2.10, (a), (b) represent phase distribution for two TC values $l = 1, 2$.

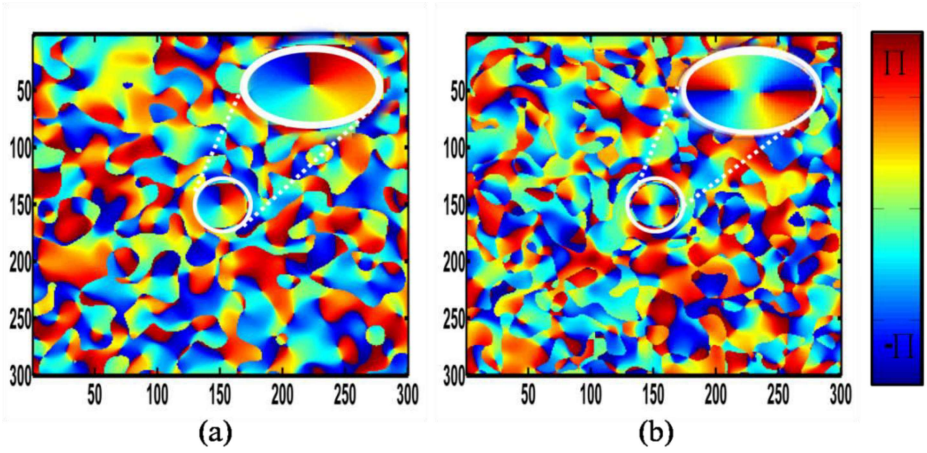

Fig. 2.10 Indicate helical phase distribution for two different cases respectively.

2.4.3 Experiment and results discussions

To experimentally demonstrate the proposed method in a lensless configuration, we designed an experimental set-up as shown in Fig. 2.11. A detailed description of the experimental method is as follows

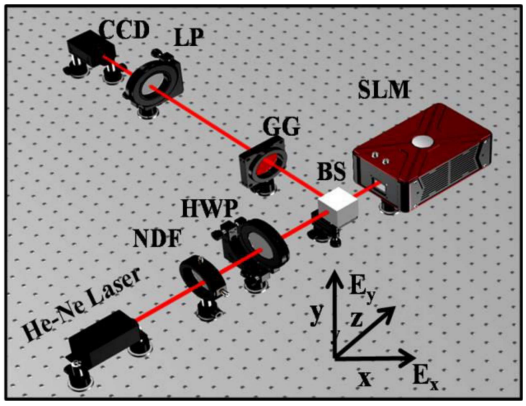

Fig. 2.11 Schematic of the experimental set-up of the proposed technique. He-Ne Laser, NDF is a neutral density filter, HWP is a half-wave plate, BS is a beam splitter, SLM is a spatial light modulator, GG is ground glass, LP is a linear polarizer, CCD is a charge-coupled device.

A spatially filtered He-Ne laser light beam with wavelength 633 nm is attenuated with a neutral density filter (NDF) and oriented at 45° with respect to the horizontal direction using a half-wave plate (HWP). The 45° polarized beam splits into two equal-intensity

beams by the 50:50 beam splitter BS. The beam transmitted from BS illuminates a phase-only SLM with a resolution of 1920 x 1080 and a pixel pitch of 8 μm (Pluto from Holoeye). The helical phase structures are displayed on the SLM and the SLM only allows modulation in the x-polarization component. Therefore, helical structure is encoded into the polarization component and the y polarization component remains intact i.e. no vortex. The beam coming from the SLM is reflected by the BS and passes through the ground glass and random scattering from the ground glass (GG) scrambles the incident light and creates a speckle pattern. The optical elements are used to measure the SPs which describe the polarization state of the randomly scattered light. The first three SPs are determined by using a polarizer and setting the transmission axis of the LP to $0°, +45°$, and $+90°$, respectively. This helps to avoid the impact of mechanically placing and rotating the QWP as is the case in conventional polarimetry. Moreover, placing the QWP in the experimental setup demands normalization of the power otherwise, SPs measurements give an error in the experimental results. The resultant field is recorded by a CCD camera with a dynamic range of 8-bit and resolution of 1280 x 1024 pixels and a pixel pitch of 4.65 micron [Thorlab model No. DCU224M]. The CCD is placed in the Fresnel regime at a distance of 250 mm from the ground glass. The CCD records the intensity speckle patterns. The recorded speckle patterns are used to determine the first three SPs using the following equations (Goldstein, 2017).

$$\begin{aligned} S_0(r) &= I(0^0) + I(90^0), \\ S_1(r) &= I(0^0) - I(90^0), \\ S_2(r) &= 2I(45^0) - S_0(r), \end{aligned} \tag{2.44}$$

where $I(\theta)$ is the intensity at the observation plane and θ is the angle of the polarizer with the x-axis. The experimentally measured SPs are used to obtain the correlations of the

fluctuations of the SPs as explained in the theory section. The experimentally measured SPs are used to determine the real part of the Stokes fluctuations correlation function by spatial averaging as a replacement for ensemble averaging.

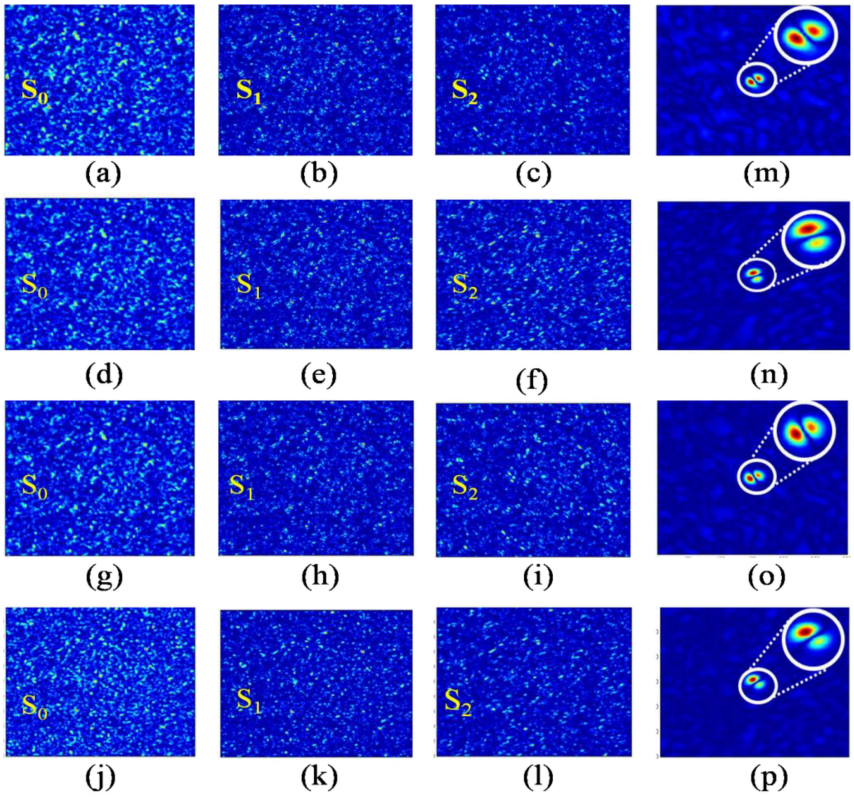

Fig. 2.12 Experimentally measured SPs (S_0, S_1, S_2) of the phase profile of the vortex beam for phase shifts of $\mathbf{0}, \boldsymbol{\pi/2}, \boldsymbol{\pi}$, and $\mathbf{3\pi/2}$ and **(m-p)** represent the corresponding real part.

The real part of the two-point polarization correlation function is evaluated from the selected Stokes fluctuations correlation. The helical phase of the coherent vortex beam is recovered from the first three Stokes parameters of the speckle pattern as explained in Eq. (2.7) and Eq. (2.43). In the experiment, a horizontal polarization component is loaded with the helical phase profile and a vertical component remains intact. These two orthogonal components travel coaxially and propagate through the random scattering medium. The intensities of the SPs (S_0, S_1, S_2) from speckles are recorded by the CCD

camera for the vortex beam with phase shifts of 0, $\pi/2$, π, and $3\pi/2$, as shown in Fig. 2.12, (a-l). The real part of the complex polarization correlation function of the experimentally measured SPs corresponding to phase shifts of $0, \pi/2, \pi$, and $3\pi/2$ are shown in Fig. 2.12, (m-p). In Fig. 2.12, (a-c), (d-f), (g-i), and (j-l) represent the first three SPs for a phase shift of 0, $\pi/2$, π, and $3\pi/2$ respectively and (m-p) shows the corresponding real part of the complex polarization correlation function.

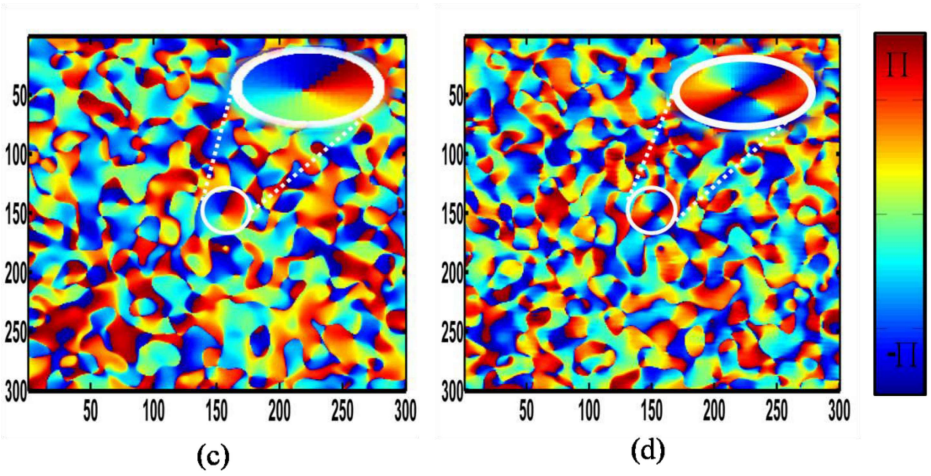

Fig. 2. 13 Experimentally recovered helical wavefront for two different cases respectively.

Figs. 2.13, (a), (b) represent phase distribution for two TC values $l = 1, 2$. This helical phase in the polarization correlation function arises due to an OAM mode in one of the orthogonal polarization components of the incoming light. For a given l, the beam indicates intertwined helical phase wavefronts, which share left-handedness (or right-handedness) with positive (or negative) l. The helical phase profile of the incident coherent beam is revealed and quantitatively estimated from the phase distribution obtained using Eq. (2.43) as shown in Fig. 2.13. Fig. 2.13 specifies the phase profile of the incident vortex beam and exhibits that the accumulated phase varies around the singularity in the order of $2l\pi$ ($l = 1, 2$, for two topological charges). This technique also

determines the helicity of the wavefront from the experimentally detected phase structure.

2.4.4 OAM mode characterization

To investigate the incident OAM modes, experimentally detected complex fields at the far field, i.e $A_l(\hat{r})\exp(il\varphi_i)$ is projected onto the spiral harmonics $e^{im\varphi}$, where *l,m* represent the TC. The complex coefficient is determined by integrating the helical wavefront of the vortex beam $A_l(\hat{r})\exp(il\varphi_i)$ with respect to the azimuthal coordinates (Molina-Terriza, 2001).

$$A_m(\Delta r) = \frac{1}{2\pi}\int_0^{2\pi} d\varphi_i \, \mathrm{e}^{-im\varphi} A_l(\hat{r}) e^{il\varphi_i}, \tag{2.45}$$

The OAM power spectrum of the vortex beam is investigated from the complex coefficient by integrating their square modulus along with the radial coordinates.

$$P(n) = \frac{1}{S}\int_0^{\infty} drr \left| A_n(\Delta r)\right|^2 . \tag{2.46}$$

where $S = \sum\int_0^{\infty} drr \left| A_m(\Delta r)\right|^2$ represents beam power and $P(l)$ indicates the OAM power spectrum.

Simulation and experimental results of the OAM distributions are shown in Fig. 2.14. Figs. 2.14, (a), (b) and (c), (d) indicate simulation and experimental results respectively. In Figs. 2.14, (a), (b) and (c), (d), the yellow and green color bars reveal the OAM distribution for two different OAM modes $l = 1,2$ respectively.

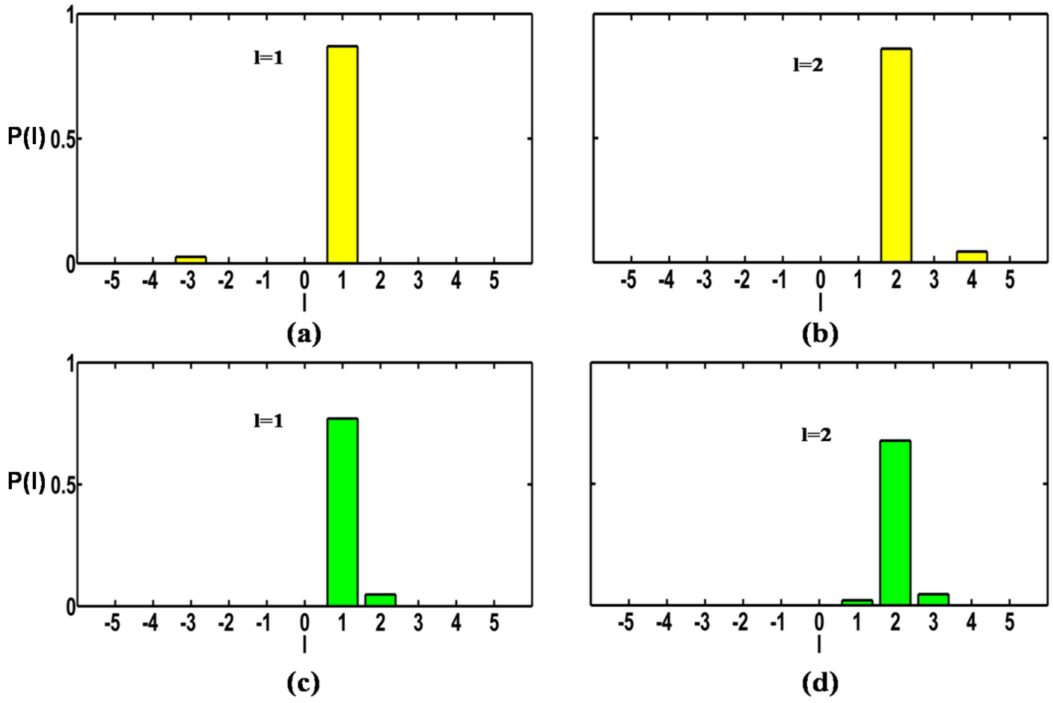

Fig. 2.14 Panels **(a, b), (c, d)** indicate simulation and experimental results for the OAM distribution for two different OAM modes $\boldsymbol{l = 1, 2}$.

2.5 Conclusion

In this chapter, we have proposed and experimentally demonstrated two different techniques to determine the OAM mode of the helical beam from the laser speckle. Theoretical analysis of the higher-order SPs correlations for the recovery of the helical OAM modes from the random light is proposed and verified by the experimental results. The proposed experimental techniques are robust due to non-interferometric and free from a separate reference beam. We have further shown the applicability of the proposed techniques experimentally by retrieving the OAM mode for different cases. The proposed techniques can faithfully retrieve the complete helical wavefront structure and OAM mode of the coherent incident light from the random speckle pattern. These techniques will be useful in imaging through random media of polarization-sensitive objects, optical communication, and characterizing random electromagnetic beams.